




Identification of the main mixing process in the synthesis of alloy nanoparticles by laser ablation of compacted micropowder mixtures

Friedrich Waag^{1,3}, Wessam I. M. A. Fares^{1,3}, Yao Li^{1,3}, Corina Andronescu^{2,3}, Bilal Gökce^{1,4}, and Stephan Barcikowski^{1,3,*} 

¹Technical Chemistry I, University of Duisburg-Essen, Universitätsstraße 7, 45141 Essen, Germany

²Technical Chemistry III, University of Duisburg-Essen, Universitätsstraße 7, 45141 Essen, Germany

³Center for Nanointegration Duisburg-Essen (CENIDE), University of Duisburg-Essen, Carl-Benz-Straße 199, 47057 Duisburg, Germany

⁴Materials Science and Additive Manufacturing, University of Wuppertal, Gaußstraße 20, 42119 Wuppertal, Germany

Received: 25 August 2021

Accepted: 13 November 2021

Published online:

3 January 2022

© The Author(s) 2021

ABSTRACT

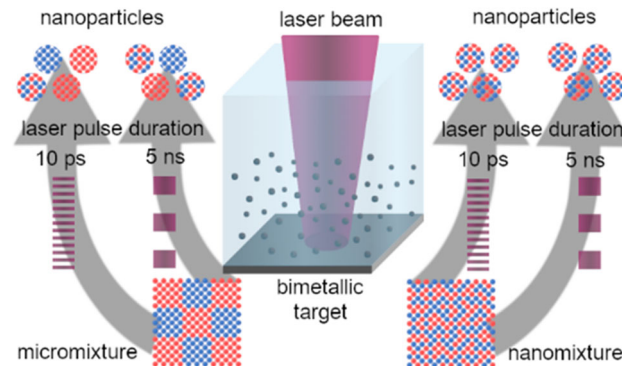
Alloy nanoparticles offer the possibility to tune functional properties of nanoscale structures. Prominent examples of tuned properties are the local surface plasmon resonance for sensing applications and adsorption energies for applications in catalysis. Laser synthesis of colloidal nanoparticles is well suited for generating alloy nanoparticles of desired compositions. Not only bulk alloys but also compacted mixtures of single-metal micropowders can serve as ablation targets. However, it is still unknown how mixing of the individual metals transfers from the micro- to the nanoscale. This work experimentally contributes to the elucidation of the mixing processes during the laser-based synthesis of alloy nanoparticles. Key parameters, such as the initial state of mixing in the ablation target, the laser pulse duration, the laser spot size, and the ablation time, are varied. Experiments are performed on a cobalt-iron alloy, relevant for application in oxidation catalysis, in ethanol. The extent of mixing in the targets after ablation and in individual nanoparticles are studied by energy-dispersive X-ray spectroscopy and by cyclic voltammetry at relevant conditions for the oxygen evolution reaction, as model reaction. The results point at the benefits of well pre-mixed ablation targets and longer laser pulse durations for the laser-based synthesis of alloy nanoparticles.

Handling Editor: Catalin Croitoru.

Address correspondence to E-mail: stephan.barcikowski@uni-due.de

<https://doi.org/10.1007/s10853-021-06731-2>

GRAPHICAL ABSTRACT



Introduction

Metal alloys shaped the history of humankind like no other class of material. Cu and Sn formed the first manmade alloy, i.e. bronze, which lent its name to an entire age of man. The increased hardness and wear resistance of bronze compared to its parent metals paved its way as a universal tool and weapon material. As history progressed, steel alloys, as the most important material class of the new age, took over. From their domination of the macroscopic world, alloys started entering the nanoscale. Intriguing properties of nanoparticles like the visible local surface plasmon resonance found for Au and Ag particles, for example, can be tuned by alloying both metals in desired compositions [1, 2]. The high specific surface, often required in catalytic processes, makes nanoparticles excellent catalysts. Particular interest lies in alloy nanoparticles, where an increased activity may be recorded for bimetallic compositions due to either a synergy between the two metals or due to ligand or electronic effects, which may affect the adsorption energy of reactants to the catalyst surface and thus the catalytic activity and selectivity [3, 4]. Besides these, variation of the composition of alloy nanoparticles can also be used to control magnetic properties [5, 6].

Several synthesis routes to colloidal alloy nanoparticles emerged [7]. Laser synthesis of colloids (LSC) represents a relatively new but high-potential synthesis method among these [8, 9]. The method has

particular strength in catalyst screening applications, as molar fraction series of alloy catalysts are easily accessible [10, 11]. In LSC, a laser beam of high intensity ablates the surface of a bulk material covered by a liquid layer, generating thus nanoparticles that disperse in the liquid. LSC enabled the synthesis of colloidal particles of various alloys, for example, brass [12], bronze [13], Ag–Cu [14], Au–Ag [15], Co–Pt [16], Fe–Rh [17], Ir–Pt [18], Ni–Pd [19], Pd–Pt [20], Pd–Y [21], and Co–Fe–Cr–Mn–Ni [22], by ablation of the corresponding bulk alloys.

Neumeister et al. synthesized homogeneous Au–Ag alloy nanoparticles by nanosecond-pulsed laser ablation of compacted mixtures of the single-metal micropowders [23]. Adjusting the ratio of single-metal Ag and Au grains in the target enabled the synthesis of alloy nanoparticles with the same composition of Ag and Au. Homogeneous alloy nanoparticles of Au and Pt, which have limited miscibility [24], were also reported by Zhang et al. by nanosecond-pulsed laser ablation of compacted micropowder mixtures of the single metals [25]. Although both studies prove mixing on the nanoscale during nanosecond-pulsed LSC of microscale metal mixtures, only limited information on how and at which stage of the process mixing occurs is provided.

It is well known that laser irradiation of colloidally mixed, single-metal nanoparticles enables the formation of alloy nanoparticles. This was demonstrated by Chen and Yeh using a nanosecond-pulsed laser for the synthesis of Au–Ag alloy nanoparticles of different compositions controlled by the mixing ratio

of Au and Ag colloids [26]. The path of alloying includes the agglomeration of single nanoparticles of both metals [27] followed by interdiffusion of Ag atoms into the Au lattice probably having core–shell intermediates [28]. Besner and Meunier later showed that the synthesis approach can also be successfully performed with femtosecond-pulsed lasers [29]. The authors also found strong indication for interdiffusion of Ag into Au. LSC is often carried out as a batch process with a long process time, which makes it difficult to distinguish between ablation and post-irradiation effects. Therefore, the formation of alloy nanoparticles due to post-irradiation often cannot be excluded in laser ablation studies.

Amendola et al. demonstrated the formation of bimetallic Au-Fe nanoparticles, solid-solution and core–shell structures, by nanosecond-pulsed LSC of thin-film stacks of the single metals performed in water or ethanol [30]. The authors exclusively observed the formation of bimetallic nanoparticles regardless of the experimental variations, which were the stacking order of the metals and the thickness of the films. In a follow-up study, the effect of nanosecond- and picosecond-pulsed LSC on the ultrastructure of the generated Fe-Au nanoparticles was investigated, this time in acetone [31]. While it was again proved that the stacking order does not influence the formation of the bimetallic nanoparticles, the study revealed that solid-solution alloy particles are formed more frequently during picosecond-pulsed LSC while core–shell particles are preferably formed during nanosecond-pulsed LSC. In both studies, the authors separated single laser pulses spatially on the stacked thin film during LSC and ablated each position on the surface only once to exclude multi-pulse effects on the target. Consequently, single laser pulses induce mixing in the ablated matter from depths of some 10 to a few 100 nm during LSC of metals.

Recently, Shih et al. investigated the dynamics of ultrashort-single-pulse LSC of nanometer-thin, stacked bilayers of Ag and Cu [32]. Their atomistic simulations predicted low elemental mixing of the two metals, independent of which element was on top. Mainly Cu- and Ag-rich nanoparticles formed during the early stage, i.e., the first 3.5 ns after the laser pulse. Their predictions were experimentally confirmed by picosecond-pulsed LSC in the same study. Interestingly, Ag–Cu alloy nanoparticles have been successfully synthesized before, but only with

nanosecond laser pulses and during conditions of multiple-pulse irradiation of the target and the colloid [14].

The just reported findings indicate mixing of atoms of different metals in nanoscale volumes of the ablated matter from the target during LSC. The boundary region of two microparticles of different metals resembles such a volume in compacted mixtures of micropowders. However, little information on intermixing in microscale volumes of the ablated matter during LSC exists. The contribution of narrow border regions to the ablated volume potentially decreases with increasing diameter of the used metal grains. The high yields of alloy nanoparticles observed by Neumeister et al. [23] and Zhang et al. [25], who used grains with up to 10 μm in diameter, indicate that either larger mixing volumes exist in the ablated matter of a single nanosecond laser pulse or that microscale mixing is a multi-pulse event.

Herein, we present an experimental study specially designed to comprehensively investigate the mixing path in alloy nanoparticle synthesis via LSC of compacted mixtures of single-metal micropowders. The Co–Fe system was explored as alloy system due to its wide-range solubility of atoms of both metals in a single crystal lattice. A molar ratio of 2:1 Fe:Co was targeted, which lies in the center of the solid-solution phase of the Co-Fe system [33]. Evaluation of the lateral mixing of the two elements was done from energy-dispersive X-ray spectroscopy (EDX) element maps recorded during scanning electron microscopy (SEM) of the surfaces of the ablation targets. We developed an analytical procedure to quantify and compare the intermixing of Co and Fe of different samples from recorded EDX element maps. For chosen samples, we investigated the chemical composition of the bulk and the surface of single nanoparticles using scanning transmission electron microscopy (STEM)-EDX and cyclic voltammetry (CV), respectively. We also report correlations of the extent of mixing with the electrocatalytic activity for the oxygen evolution reaction (OER).

Materials and methods

Laser synthesis of colloids experiments

Nanoparticle colloids were produced using a picosecond- and a nanosecond-pulsed Nd:YAG laser

system each operated at the fundamental wavelength of 1.064 nm. The picosecond-pulsed laser (Atlantic; Ekspla, Vilnius, Lithuania) was used at a pulse length of 10 ps, a pulse repetition rate of 100 kHz, and an average power of 10 W. The pulse energy was 0.1 mJ. The nanosecond-pulsed laser (Powerline E20; Rofin-Sinar, Plymouth, United States) was used at a pulse length of 5 ns, a repetition rate of 10 kHz, and an average power of 5 W. The pulse energy was 0.5 mJ.

For LSC, the target was placed into a glass vessel and was covered with a 4 mm layer of ethanol corresponding to a volume of 8 ml. Ethanol was chosen in order to limit the oxidation of Co and Fe during LSC. The laser beam scanned the target surface in spiral patterns with a 3 mm diameter and a scanning speed of 4 m s^{-1} . An f-theta lens with 100 mm focal length was used to focus the circular, Gaussian laser beam. We varied the following experimental parameters: initial state of mixing of the target, ablation time, laser spot diameter, and laser pulse duration (Fig. 1). All these parameters may affect if and on what scale atoms of Co and Fe mix during LSC. We explain the possible effects in the specific results sections. Variation of the laser spot size on the target surface was done by changing the distance between the lens and the target surface. In each LSC experiment, 30 s of ablation were applied if not mentioned differently. For longer ablation times, the liquid volume was replaced every 30 s.

The laser spot diameter was calculated at a level of e^{-2} of the laser energy density, assuming an ideal Gaussian laser beam. Light refraction of the air-ethanol interface was considered. All laser beam

parameters were extracted from the manufacturer's documentation.

Preparation of ablation targets

The ablation targets were prepared using micropowders of Co (1.6 μm , 99.8%, metals basis; Alfa Aesar, Ward Hill, United States) and Fe (Spherical, < 10 μm , 99.9+%, metals basis; Alfa Aesar, Ward Hill, United States). For a single ablation target, a 1 g mixture of Co and Fe was used while using a molar ratio of 2:1 (Fe:Co). The average grain sizes (weighted by cross-section) of 0.9 μm (Co) and 2.3 μm (Fe) for the micropowders of Co and Fe, respectively (Fig. 2a, b), was determined using SEM. The powder mixtures of each target were mechanically mixed for 10 min and were further compressed to cylindrical pellets of a diameter of 13.5 mm and a thickness of 1.35 mm using a pressure of 560 MPa. One target was heat-treated at 1,000 °C in Ar at atmospheric pressure for 20 h to initiate diffusive mixing of Co and Fe on the nanoscale. Slight surface oxidation was found after the heat treatment. The oxide layer was mechanically removed prior to LSC by polishing with super fine sandpaper (P1200). In this manuscript, the compacted powder mixture is labeled as raw target, and the additionally heat-treated mixture is labeled as sintered target. EDX analysis demonstrates the different initial states of mixing in both types of targets (Fig. 2c).

Analysis of micropowders and ablation targets

The morphology and size distributions of the micropowders were investigated using SEM (XL30; Philips, Amsterdam, Netherlands). All samples were fixed with double-sided adhesive and conductive patches attached to aluminum sample holders. EDX element maps were recorded at magnifications of 500x (two per parameter set) and 1000x (one per parameter set). The acceleration voltage was 15 kV. 64 frames with 512 px \times 400 px were sampled. The analyzed areas had dimensions of 256 μm \times 200 μm (magnification of 500x) and 128 μm \times 100 μm (magnification of 1000x). All maps were quantitatively analyzed as described in the next two paragraphs. The results obtained from the 500x-maps are presented in the main manuscript, and those extracted from the 1000x-maps are shown in the

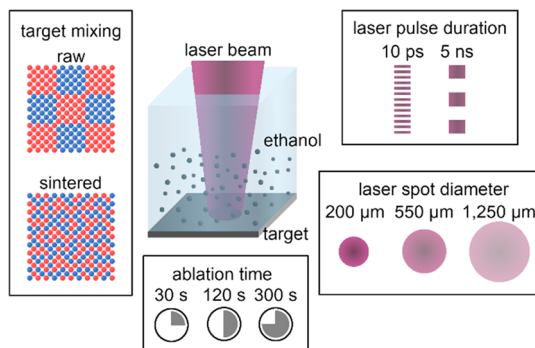


Figure 1 Overview of the experimentally performed parameter variations. Varied parameters are the initial state of mixing of the target, the laser pulse duration, the laser spot diameter, and the ablation time.

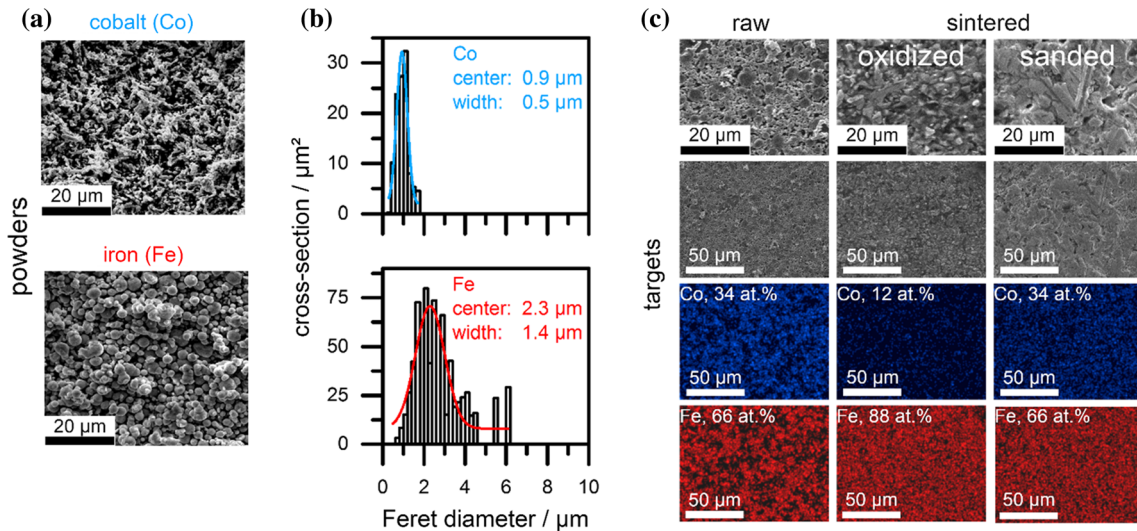


Figure 2 Metal micropowders and ablation targets. Secondary electron SEM images of the used metal powders (a), their size distributions weighted by the cross-section (b), and secondary

electron SEM images as well as EDX element maps of a raw target, a sintered target with oxidized surface, and a sintered target after sanding (c). In (b), lognormal fits were applied.

Supplementary Material (Figure S1). The exemplary element maps shown in the figures of the manuscript were recorded at 1000x magnification.

The software Fiji (Fiji contributors) was used to transform the element maps (Fig. 3a) to binary images (Fig. 3b, c), in which white pixels mark the detection of the element and black pixels resemble the background. (Multiple detections of one element in a single pixel of the map cannot be processed by

the EDX software.) The binary maps were separated into boxes of 16 px × 16 px, representing 8 μm × 8 μm (magnification of 500x) or 4 μm × 4 μm (magnification of 1,000x), and the number of white pixels was counted in each box (Fig. 3d, e). We used a code written in LabVIEW (National Instruments, Austin, United States) for this operation. Characteristic X-rays were generated in a sample volume of approximately 0.5 to 1 μm in diameter [34], which

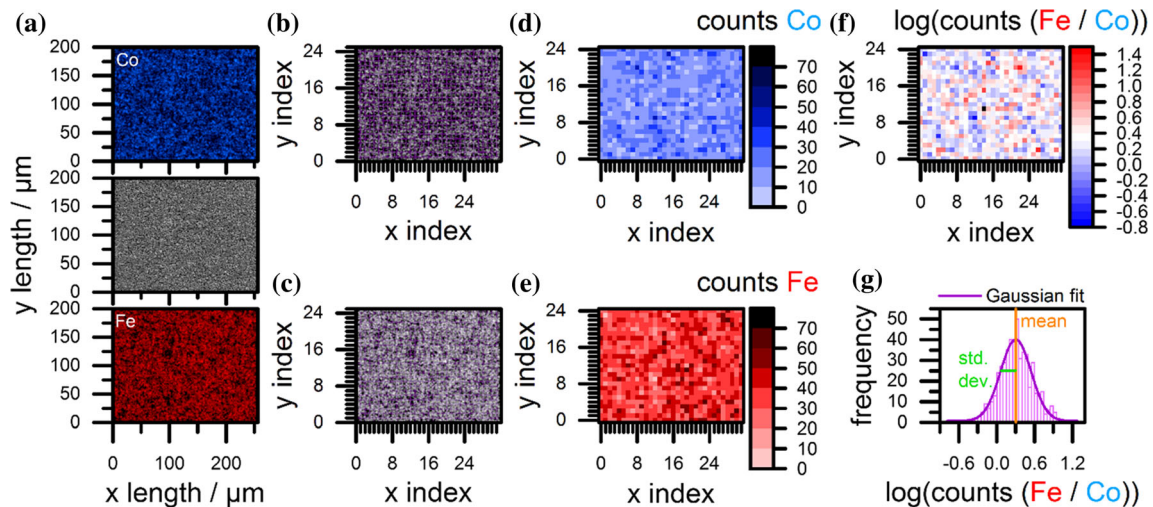


Figure 3 Extraction of the extent of mixing from element maps. Secondary electron SEM image and element maps of the target surface (a), binary transformations of the element maps of Co (b) and Fe (c) with indexing grids, counts of white pixels related to Co (d) and Fe (e) in indexed boxes of the grids, logarithmic count

ratio in indexed boxes (f), and frequency distribution of different log count ratios in the grid (g). In (g), a Gaussian fit and its distribution parameters standard deviation (std. dev.) and mean value (mean) are shown.

corresponds to the lateral resolution limit of the applied SEM–EDX analysis. The box size of the image processing of the EDX element maps should be well above that limit. All atomic fraction data of Co and Fe determined by EDX are estimated to be accurate to ± 1 at.%. The logarithm of the ratio of counts of Fe and Co was calculated for all single boxes (Fig. 3f). We numerically analyzed the frequency of specific logarithmic count ratios and fitted Gaussian distributions (Fig. 3g). The mean value of the distribution represents the average composition. A mean value of 0.3 corresponds to the expected Fe:Co ratio of 2:1 (logarithm). The standard deviation represents the range of compositions. Low values represent good mixing of Co and Fe.

For the analysis of the size of the ablation areas, i.e., craters, on the targets (after 1 s of ablation for the picosecond laser and 10 s of ablation for the nanosecond laser), a light microscope (CX40; Olympus, Tokyo, Japan) was used in reflection mode. The ablation areas and the average grain cross-section were used to calculate the number of grains per spot. The average grain cross-section calculated from the grain size distributions (Fig. 2b) was $4 \mu\text{m}^2$. Spherical grains were assumed, and porosity was not considered. About 205 Co grains and 224 Fe grains were measured from secondary electron SEM images. The number of metal grains per spot was calculated using the ablation area diameter assuming circularity.

Analysis of nanoparticles

The size distributions of the laser-generated nanoparticles were determined from micrographs recorded with a transmission electron microscope (TEM, JEM-2200FS; JEOL, Akishima, Japan). More than 500 nanoparticles were analyzed for each sample in the present study. The chemical composition of single nanoparticles was extracted from (STEM-)EDX element maps. We analyzed only isolated particles, which had diameters of 5 to 150 nm with an average diameter of 35 nm. A minimum of 20 particles per sample was analyzed. The average was 27. A dependence of the composition on the particle size was not found. Mean values and standard deviations of the distributions of compositions of single nanoparticles of a sample were calculated descriptively.

Electrochemical characterization of the nanoparticles

All electrochemical experiments were performed using a potentiostat (VersaSTAT 3F; AMETEK, Berwyn, United states). The rotating disk electrode (RDE) technique was used to evaluate the surface composition of the synthesized Co–Fe nanoparticles as well as their oxygen evolution reaction (OER) electrocatalytic activity. The measurements were performed in 0.1 M KOH using a three-electrode setup containing a RDE made of glassy carbon as a working electrode, a Ag/AgCl 3 M KCl electrode as reference electrode and a Pt wire as counter electrode. 4.9 mg nanoparticles supported on C (20 wt%) were dispersed by sonication in 5 mL isopropanol:MilliQ water solution (50/50 v/v) containing 40 μL Nafion solution. A certain volume of the resulting ink was used to drop coat a uniform catalyst film on the electrode with a mass loading of 0.05 mg cm^{-2} . The electrochemical measurements were performed by cyclic voltammetry (CV). An initial potential of -1 V vs. Ag/AgCl 3 M KCl was applied and was further increased by scanning in the anodic direction with a scan rate of 5 mV s^{-1} up to a vertex potential of 1 V vs. Ag/AgCl 3 M KCl. All potentials were measured with respect to Ag/AgCl 3 M KCl reference electrode and later converted to the RHE scale using the following equation:

$$E_{\text{RHE}} = E_{\text{Ag/AgCl 3 M KCl}} + E_{\text{Ag/AgCl 3 M KCl}}^0 + 0.059 * \text{pH}$$

where $E_{\text{Ag/AgCl 3 M KCl}}$ is the applied potential vs. the reference electrode, $E_{\text{Ag/AgCl 3 M KCl}}^0$ represents the potential of the Ag/AgCl 3 M KCl reference electrode (0.21 V) with respect to the normal hydrogen electrode, and the pH value was approximated to be 13. The experiments were performed three times for each material to ensure the reproducibility of the experiment.

Results and discussion

Laser spot diameter and the initial mixing state of the target

We started our study by evaluating the influence of the laser spot diameter used during the LSC of a raw (compacted micropowder mixture) and of a sintered ablation target. The laser spot size was changed by

variation of the distance between the focusing lens and the ablation target. Three characteristic positions were chosen: (1) close to the focus, (2) at the highest nanoparticle productivity, and (3) at the maximized ablation area. We used picosecond laser pulses and ablated for 30 s. Targets with two different initial states of mixing were used to test for segregation processes during LSC.

We induced a change in the number of metal grains in the laser spot by variation of the laser spot size and thus increased the probability of achieving the desired composition of both metals in the total ablated matter. Additionally, the laser energy density was decreased when larger spot diameters were applied. As demonstrated in our previous study, the heat loss in the ablation target during picosecond-pulsed LSC strongly depends on the energy density of the laser pulse [35]. Table 1 shows the impact of the laser spot diameter on the relevant experimental parameters. In addition, we found the threshold energy density for ablation of the used targets to be in the range of 0.05 to 0.2 mJ cm⁻².

Figure 4a shows secondary electron SEM images and element maps of the ablation area on the surface of a raw and a sintered target using a laser spot diameter of 1250 μm. No difference was found when using the other laser spot diameters. The topographies of raw and sintered targets differed in their appearance after LSC. Figure S2 shows larger SEM images of the target topographies. In both topographies, the laser-induced periodic structures and micron-sized bumps can be observed, with a more homogeneous bump size in the case of the sintered target. In the case of the raw target, some bumps looked similar to the initial grains indicating that material transport on the microscale was limited in the target during LSC.

The element maps (Fig. 4a) indicate no change in the extent of mixing during LSC for both types of targets in relation to the non-ablated ones (Fig. 2c). The corresponding distributions of the count ratios

confirm this observation (Fig. 4b), as shown by the extracted standard deviations (Fig. 4c). Furthermore, they confirm the better initial state of mixing in sintered targets compared to raw ones. We relate the variations of the mean value (Fig. 4d), which were much stronger for the raw target, to a more inhomogeneous composition.

In conclusion, we found stronger mixing of Co and Fe in the sintered targets compared to the raw ones. The initial state of mixing preserved during picosecond-pulsed LSC in ethanol regardless of the applied laser spot diameter. The number of metal grains contributing to a single ablation pulse and the laser energy density had no apparent effect on the mixing of Co and Fe in the target. This was probably due to the high values of grains per spot at all parameter sets (Table 1), that statistically guaranteed the abundance of both metals in the ablated material. A missing effect due to stronger heat loss in the target at lower laser energy densities (larger laser spots) was most likely related to the ultrashort pulse duration.

Variation of the ablation time and the laser pulse duration

Further, we investigated the effect of the ablation time and the laser pulse duration during LSC. The laser spot diameter was 550 μm and a raw target was used. Time plays an essential role in conventional mixing processes, which we addressed with the ablation time. The pulse duration strongly influences the interaction of the target and the laser pulse. Laser-excited electrons transfer their energy to lattice phonons in a timeframe of hundred femtoseconds to single picoseconds [36, 37]. Nanosecond pulses therefore have a much stronger thermal impact on a metal target than short picosecond pulses [38, 39].

Figure 5a shows secondary electron images and element maps of the target surface after 300 s ablation time. No difference was found when shorter ablation times were applied. For picosecond pulses, the

Table 1 The values of relevant LSC parameters during LSC as a function of the laser spot diameter

Laser spot diameter (μm)	Ablation area diameter (μm)	Metal grains per spot (-)	Laser energy density (mJ cm ⁻²)
200	400	31,000	89
550	700	93,000	11
1250	1200	276,000	2

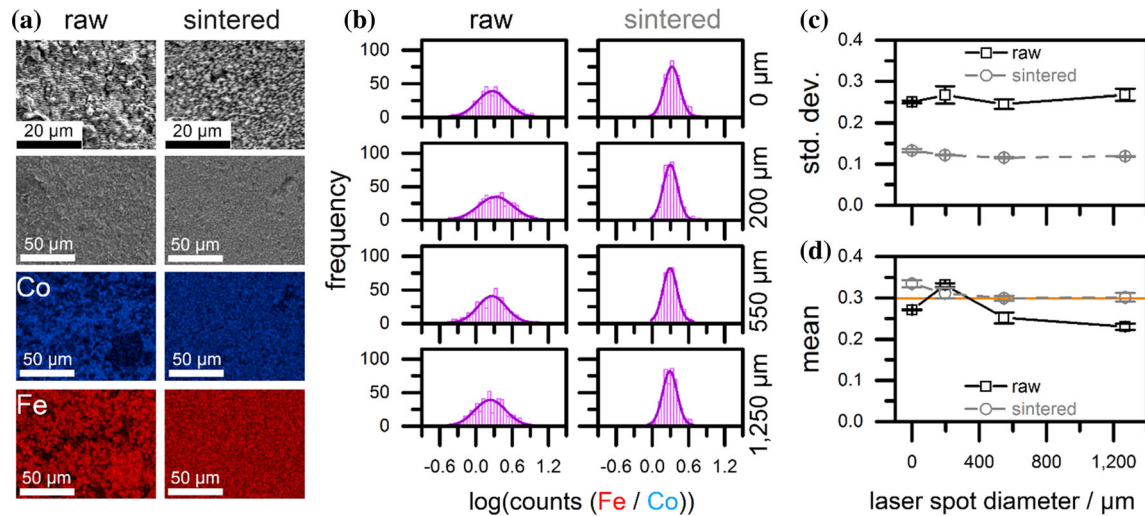


Figure 4 Variation of the laser spot diameter and the initial mixing state of the target. Secondary electron SEM images and EDX element maps of a raw and a sintered target after picosecond-pulsed LSC with a laser spot size of 1250 μm (a), frequency distributions of logarithmic count ratios calculated from element maps (b), and the distribution parameters standard deviation (std. dev, c) and mean value (mean, d) extracted from the Gaussian fits

of the frequency data versus laser spot diameter. In (b), frequency data and corresponding Gaussian fit of one representative pair of element maps per parameter set are shown. In (d), the orange line marks the ideal Fe:Co log ratio of 0.3. In (c, d), error bars represent the maximum deviation from the average of two measurements at different positions. 0 μm represents the case of no ablation.

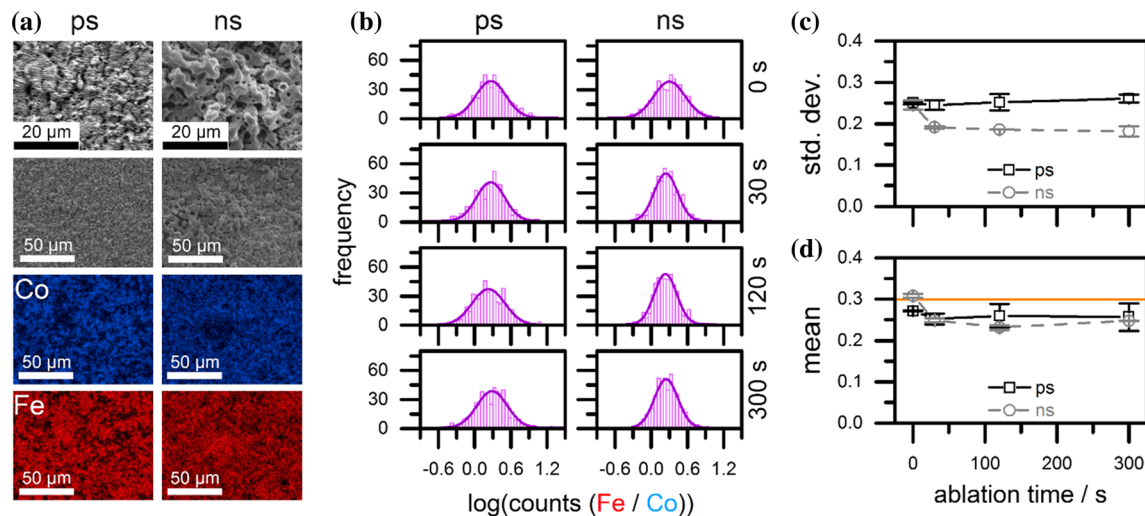


Figure 5 Variation of the ablation time and the laser pulse duration. Secondary electron SEM images and EDX element maps of a raw target after 300 s of picosecond- and nanosecond-pulsed LSC (a), frequency distributions of logarithmic count ratios calculated from element maps (b), and the distribution parameters standard deviation (std. dev, c) and mean value (mean, d) extracted from the Gaussian fits of the frequency data versus the ablation

time. In (b), frequency data and corresponding Gaussian fit of one representative pair of element maps per parameter set are shown. In (d), the orange line marks the ideal Fe:Co log ratio of 0.3. In (c, d), error bars represent the maximum deviation from the average of two measurements at different positions. 0 s represents the case of no ablation.

topography resembled the one found on the raw target after 30 s LSC with a laser spot diameter of 1,250 μm (Fig. 4a). After nanosecond-pulsed LSC, we found a network of frozen melt structures on the raw

ablation target, indicating material transport. Pores and height differences in the topography appeared larger after nanosecond-pulsed LSC.

The element maps (Fig. 5a) show apparent differences in the extent of mixing induced by picosecond and nanosecond laser pulses. After picosecond-pulsed LSC, Co and Fe remained well separated and could be assigned to clear microstructures as already observed during the variation of the laser spot diameter. The reader is also referred to the high-magnification element maps in Figure S3. The nanosecond pulses induced mixing of Co and Fe in the target, but some inhomogeneity remained in the composition on the microscale. The distributions of the count ratios of Co and Fe (Fig. 5b) as well as the extracted standard deviations of the Gaussian fits (Fig. 5c) underline the observations. In nanosecond-pulsed LSC, the extent of mixing already improved during the first 30 s of ablation and remained unchanged at longer times. The improvement of mixing was less strong than what we observed during target sintering (Fig. 4c). No clear dependence between the standard deviation (Fig. 5c) and the mean value (Fig. 5d) was found.

In conclusion, nanosecond pulses led to a strong structural change in the target topography in contrast to picosecond pulses, where no structural change was found. The appearance of the target surface after nanosecond-pulsed LSC suggested its origin in melt processes. Microscale mixing accompanied the structural changes of the ablation target. The target topography and the extent of mixing experienced no further changes for ablation times longer than 30 s. However, the extent of mixing achieved by sintering was not reached. Consequently, the mixing processes were slower than the material removal rate.

Variation of the initial mixing state of the target and the laser pulse duration

As discussed in the previous two results sections, pre-LSC sintering and LSC with nanosecond laser pulses influenced the extent of mixing in the ablation target the strongest. In this section, we compare the effect of both parameters on the extent of mixing in the targets as well as in the generated nanoparticles in more detail. Moreover, we include nanosecond-pulsed LSC of a sintered target to the consideration. In the comparison, the parameters ablation time and laser spot diameter remained constant at 30 s and 550 μm , respectively.

The laser pulse duration and the initial state of mixing of the target influenced the topography of the

target surface after LSC (Fig. 6a and Figure S2). More regular structures emerged on the sintered target and larger pores evolved during nanosecond-pulsed LSC. The grains of the raw target formed a solid structure mainly due to friction between single grains and only partly due to sinter bridges induced by powder compression. Moreover, thin oxide layers covered the surfaces of the grains. Consequently, laser-induced heat accumulated in grains close to the target surface during LSC and probably led to the formation of different structures during LSC of raw compared to sintered targets. In addition, the differences in the initial porosity of raw and sintered targets and their different mechanical strengths may have contributed to the laser-induced structures.

Nanosecond pulses had a clear thermal impact on the raw target. Frozen melt structures appeared. Merging of initial pores to larger ones potentially accompanied the fusion of metal grains. The irregular structure further favored inhomogeneous ablation and the formation of the large differences in height. The laser-made structure on the sintered target differed from the one observed on the raw target. Still, it had large pores and height differences but appeared more regular. The strong height differences in the case of the raw target could have also been influenced by the higher initial porosity and the lower mechanical strength. Creating a high target density (low porosity) by sintering the target is key to avoid mechanical ablation side effects, as has been reported by Schmitz et al. [40].

The element maps (Fig. 6a) illustrate that the applied picosecond pulses induced no mixing of Co and Fe on the resolvable scale of the maps. At the applied conditions, nanosecond pulses induced mixing but to a lower extent than could be realized by solid-state sintering. The extracted standard deviations of the Gaussian fits of the frequency distributions of the log count ratios (Fig. 6c) demonstrate that the high extent of mixing of the sintered target was preserved during LSC with both pulse durations. Only slight deviations from the ideal mean occurred.

The composition of single nanoparticles generated during the different experiments was analyzed (Fig. 6b). Nanoparticles containing Co as well as Fe were formed in all samples, independent of the used target or laser, validating the successful synthesis of Co–Fe alloy nanoparticles by LSC in ethanol. The Supplementary Material contains additional EDX

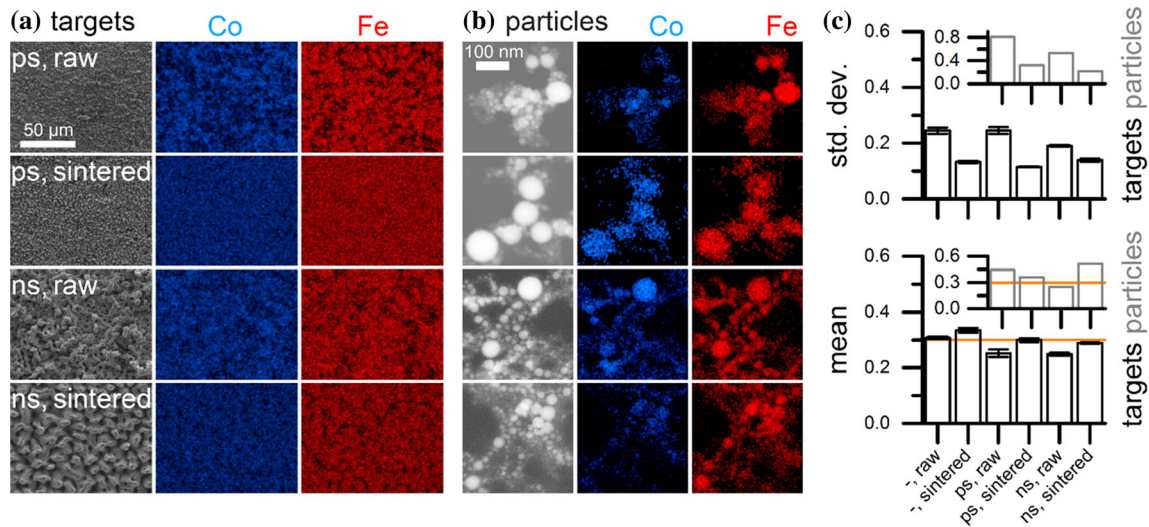


Figure 6 Variation of the initial mixing state of the target and the laser pulse duration. Secondary electron SEM images and EDX element maps of a raw and a sintered target after 30 s of picosecond- and nanosecond-pulsed LSC with a laser spot diameter of 550 μm (a), STEM images and element maps of nanoparticles produced during the different LSC experiments (b), and the distribution parameters standard deviation (std. dev, top)

element maps of the samples that underline the results (Figure S4). A similar trend regarding the narrowness (standard deviation) of the range of single-particle compositions was found as for the standard deviation of the extent of mixing of the target surfaces after LSC (Fig. 6c). This highlights that the LSC-induced mixing of Co and Fe in the target determined the quality of the synthesized nanoparticles.

We found almost exclusively spherical nanoparticles with diameters in the range of a few nanometers

and mean value (mean, bottom) of the frequency distributions of logarithmic count ratios calculated from element maps of the targets and single nanoparticles (c). In (a, b), all images have the same scale as the respective first image. In (c, bottom), the orange line marks the ideal Fe:Co log ratio of 0.3. In (c), the bar symbol (–) in the x -scale labels identifies the targets which were not laser-irradiated.

up to 150 nm in all samples (Fig. 7a, b and Figure S5). More than 90% of the particles were smaller than 30 nm with a mean value of 8 to 10 nm. We also could not observe any differences between the nanoparticles of the different samples neither in their size distribution nor in the ultrastructure. The EDX element maps of the nanoparticles in Fig. 6b and Figure S5 show that Co and Fe were homogeneously distributed in individual particles in all samples. However, single particles with more strongly oxidized shell compared to the core were also found, as

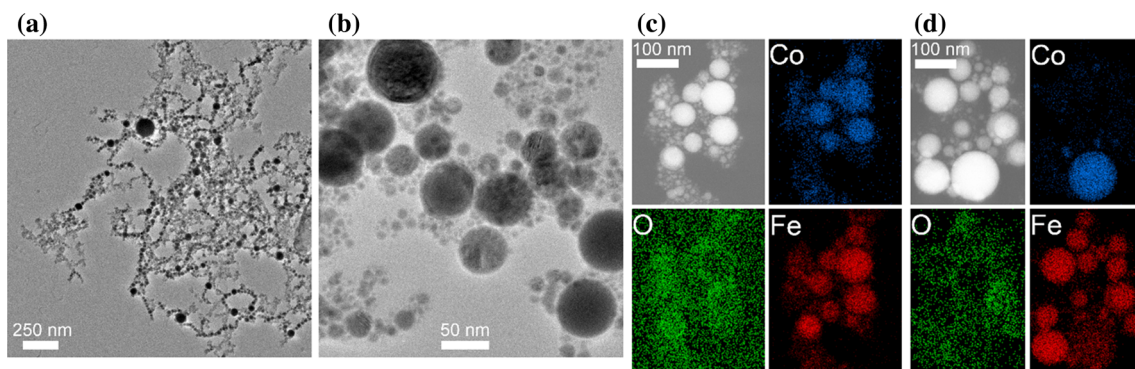


Figure 7 Morphology and ultrastructure of Co–Fe nanoparticles. Exemplary TEM images of laser-generated Co–Fe nanoparticle at 10kx (a) and 60kx (b) magnification, exemplary STEM images and EDX element maps of nanoparticles produced by picosecond-

pulsed LSC of a sintered (c) and a raw (d) target, including surface-oxidized particles as indicated by the EDX oxygen signal. Note that we also found surface-oxidized particles produced by nanosecond-pulsed LSC.

shown by the EDX element maps in Fig. 7c, d. The surface oxides were Fe-rich. Selective oxidation of Fe was not surprising due to its higher oxygen affinity. Similar element-specific surface oxidation has recently been reported for laser-generated Mn-rich high entropy alloy metallic glass nanoparticles, where the slight manganese oxide/hydroxide surface segregation has been observed, which increased with Mn content in the alloy [41].

Despite using ethanol as a dispersant, we were able to detect oxygen in the Co–Fe nanoparticles (Fig. 7c, d). Variation of the dispersant is an important tool for structure manipulation in the synthesis of colloidal nanoparticles by LSC, especially in the synthesis of nanoparticles of reactive metals. For example, Amendola et al. demonstrated the formation of iron-based nanoparticles (metal, oxides, and carbide) during the nanosecond-pulsed laser ablation of Fe in different organic solvents [42]. Kanitz et al. did similar experiments utilizing a femtosecond-pulsed laser [43]. The authors found a lower extent of oxidized Fe in nanoparticles prepared in acetone compared to ethanol. In addition, they observed more iron carbide in acetone compared to ethanol. In case of Co, Chen et al. found that nanosecond-pulsed laser ablation of the metal in ethanol leads to much less oxidized nanoparticles compared to water [44]. The formation of Co carbide nanoparticles was observed by Zhang et al. during the nanosecond-pulsed laser ablation of cobalt in acetone [45]. More recently, Nadarajah et al. systematically investigated the suppression of nanoparticle oxidation in both acetone, which contains oxygen in its molecular structure, and acetonitrile, which is an oxygen-free molecule, by degassing and drying the organic solvents [17]. They found that independent of the solvent, a combination of both solvent purification methods leads to oxidation-minimized Fe–Rh nanoparticles, proven even by atom probe tomography, and no impact of the bound oxygen in the molecule of the organic solvent could be found. But Johny et al. recently discovered that acetonitrile as dispersant leads to amorphous (metallic glass) nanoparticles if a quinary or senary alloy is ablated and discussed the role of solvent-delivered carbon as glass morphology stabilizer [41]. This amorphization phenomenon was not observed for quinary alloy nanoparticles produced by laser ablation in ethanol [46].

To qualitatively and statistically investigate the surface composition of the nanoparticles synthesized

by LSC using different pulse durations as well as raw or sintered targets, CV was used. Considering that previously to the measurement, the samples were exposed to the air, surface oxidation cannot be excluded. Therefore, we decided to apply a reductive potential (-1 V vs. Ag/AgCl 3 M KCl) prior to the CV measurement. We then increased the potential with a scan rate of 5 mV s^{-1} in the anodic direction up to 1 V vs. Ag/AgCl 3 M KCl aiming to identify possible oxidation processes of Co on the nanoparticle surface (Fig. 8). Considering the relatively high amount of Fe in the targets used for LSC (Fe:Co = 2:1), we did not expect any oxidation peak to be visible in the CVs [47]. Still, for the raw target, a clear oxidation peak, more pronounced in the case of nanosecond pulses, is observed at $\sim 1.2 \text{ V}$ versus RHE, which can be attributed to the $\text{Co}^{2+}/\text{Co}^{3+}$ oxidation. Previous reports show that the potential at which Co^{2+} oxidation to Co^{3+} occurs is strongly influenced by the Fe:Co ratio and shifts to more anodic potentials with increased Fe concentration [48]. This indicates a difference in the composition of the surface of the nanoparticles compared to the composition of the overall target. Considering the relative intensity of the $\text{Co}^{2+}/\text{Co}^{3+}$ oxidation peak, it can be concluded that a slightly higher Co amount is electrochemically active in nanoparticles produced from raw targets than from sintered targets and in nanoparticles synthesized by nanosecond-pulsed LSC than by picosecond-pulsed LSC. Nanoparticles produced by picosecond-pulsed LSC from sintered targets show no visible $\text{Co}^{2+}/\text{Co}^{3+}$ oxidation peak indicating that the best Co and Fe mixing is achieved. This

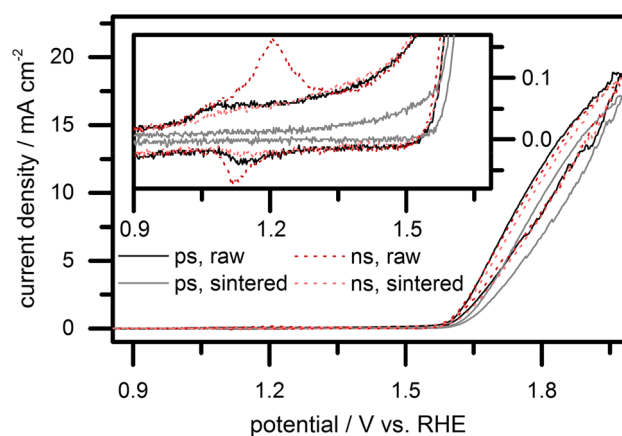


Figure 8 Electrochemical data. Cyclic voltammograms recorded using the synthesized Co–Fe nanoparticles using RDE technique in 0.1 M KOH using a scan rate of 5 mV s^{-1} .

observation is in line with the conclusion extracted from the EDX element maps (Figs. 4b, 6c), where better mixing was observed when sintered targets were used.

The availability of an increased amount of Co on the nanoparticles' surface is confirmed also by the OER catalytic performance. While Fe is the active site for OER, the in situ formed FeOOH shows poor conductivity compared to CoOOH, and therefore Fe-rich catalyst films often show inferior electrocatalytic activity compared to Co-rich ones. Still, the small compositional difference observed for the four investigated systems does not seem to significantly impact the OER electrocatalytic activity. The small differences were expressed in slightly lower activities of the nanoparticles from the sintered targets with the lowest value for the particles from the picosecond-pulsed LSC. Since all samples had very similar particle size distributions (Figure S5) and were processed in the same way to heterogeneous catalysts, the deviations could be due to the homogeneity of the composition of individual particles. It is possible that the selected Fe:Co ratio of 2:1 is not optimal for maximum OER activity. In that case, greater heterogeneity in particle composition, as achieved during ablation of raw targets, could be beneficial for higher activity. It would be interesting to investigate this aspect further in follow-up studies.

Mixing processes during LSC

We can conclude that the mixing of Co and Fe mainly occurred in the laser-irradiated and heat-affected but initially not ablated parts of the target. Mixing during the ablation process and the particle formation from ablated material contributed only to a low extent to the generation of alloy nanoparticles (Fig. 9).

During ultrashort-pulsed LSC, we could not detect any mixing of Co and Fe in the raw ablation target at the micrometer level, yet we found alloy nanoparticles, albeit with very different compositions. We conclude that material from neighboring grains could mix during ablation, but presumably only in a very short period of time and thus only in very small volumes. This is in agreement with the results of Shih et al. mentioned earlier, who found limited mixing of Ag and Cu from a few nanometer-thick layers in their atomistic models and in subsequent experiments [32]. Note that the authors focused their study on material transport processes along the propagation direction

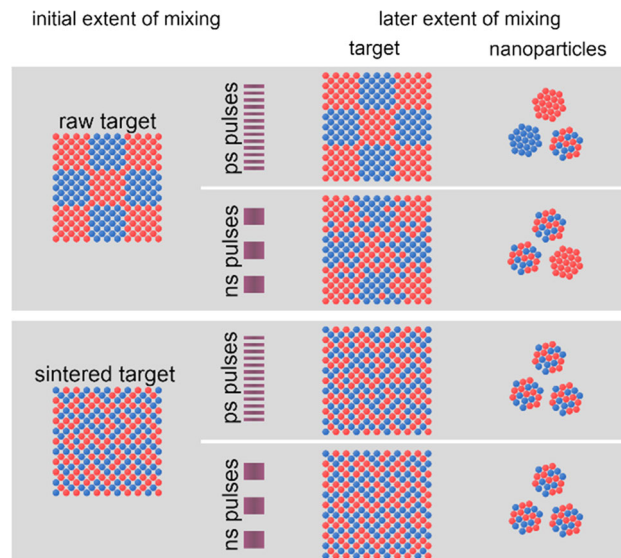


Figure 9 Schematic illustration of the effect of picosecond and nanosecond laser pulses on the extent of mixing of bimetallic ablation targets and laser-generated nanoparticles.

of the laser beam. Our interest was in material transport in the perpendicular direction across the border of neighboring micrograins.

The applied nanosecond laser pulses visibly changed the topography of the ablation targets during LSC and induced the transport of melted, non-ablated material on the microscale. The extent of mixing of Co and Fe in the ablation target reached an optimum already after 30 s LSC but was still far from the quality we achieved by solid-state sintering. Thus, the melted, non-ablated material did not have sufficient time and energy to reach the thermodynamically desired extent of mixing until its ablation. The layer of melted, non-ablated material probably reached only a few micrometers deep into the metal target after one short nanosecond pulse and was probably ablated by the subsequent one or two pulses irradiating the same position [49]. A higher extent of mixing during nanosecond-pulsed LSC should be achievable by either decreasing the laser energy density or increasing the pulse duration to increase the thermal impact on the target.

Conclusion

The compositionally controllable properties of alloy nanoparticles make them interesting for many applications, especially in (optical) sensing and

catalysis. Our results demonstrate that different approaches of LSC yield alloy nanoparticles. However, the amount of alloy nanoparticles in the total colloid as well as the range of compositions of single particles differ significantly. We achieved the best results, i.e., the highest yield of alloy particles with the narrowest composition range, by laser ablation of a sintered target, regardless of the laser pulse duration. Consequently, targets with element mixing on the nanoscale should be used to synthesize multi-element nanoparticles if possible. However, since not all elements can be easily mixed on the nanoscale in all conceivable compositions, ablation targets with microscale elemental segregation must be used in some cases for the generation of alloy nanoparticles by LSC. Such targets should be processed with nanosecond pulses to increase the yield and quality of alloy nanoparticles.

In all experiments, the extend of mixing of Co and Fe in the target after LSC corresponded well to the homogeneity of the composition of the nanoparticles. A good mixture of the elements in the target indicated a narrow composition range of the generated alloy nanoparticles. We, therefore, conclude that during LSC, mixing processes with significant material transport over micrometer distances take place only in the ablation target and only when sufficiently long laser pulse lengths are applied.

The influence of the laser pulse length on material transport processes in the ablation target should be further investigated in future studies. It is of particular interest if transport processes can be intensified with longer pulse durations or lower energy densities (for nanosecond pulses) and if there is a minimum pulse length required to start these processes.

Acknowledgements

The authors thank Jurij Jacobi and the Interdisciplinary Center for Analytics on the Nanoscale (ICAN) for TEM measurements.

Funding

Open Access funding enabled and organized by Projekt DEAL. We gratefully acknowledge funding by the German Federal Ministry of Education and Research (03SF0497B). BG further acknowledges

funding from the German Research Foundation (DFG) within the CRC/TRR 270 (405553726, B08), the Heisenberg program (445127149, GO 2566/10-1) and project GO 2566/2-1.

Declarations

Conflict of interest The authors declare that they have no conflict of interest.

Supplementary Information: The online version contains supplementary material available at <http://doi.org/10.1007/s10853-021-06731-2>.

Open Access This article is licensed under a Creative Commons Attribution 4.0 International License, which permits use, sharing, adaptation, distribution and reproduction in any medium or format, as long as you give appropriate credit to the original author(s) and the source, provide a link to the Creative Commons licence, and indicate if changes were made. The images or other third party material in this article are included in the article's Creative Commons licence, unless indicated otherwise in a credit line to the material. If material is not included in the article's Creative Commons licence and your intended use is not permitted by statutory regulation or exceeds the permitted use, you will need to obtain permission directly from the copyright holder. To view a copy of this licence, visit <http://creativecommons.org/licenses/by/4.0/>.

Supplementary Information: The online version contains supplementary material available at <http://doi.org/10.1007/s10853-021-06731-2>.

References

- [1] Link S, Wang ZL, El-Sayed MA (1999) Alloy formation of gold–silver nanoparticles and the dependence of the plasmon absorption on their composition. *J Phys Chem B*. <https://doi.org/10.1021/jp990387w>
- [2] Beyene HT, Chakravadhanula VSK, Hanisch C, Elbahri M, Strunskus T, Zaporojtchenko V, Kienle L, Faupel F (2010) Preparation and plasmonic properties of polymer-based composites containing Ag–Au alloy nanoparticles produced by vapor phase co-deposition. *J Mater Sci*. <https://doi.org/10.1007/s10853-010-4663-5>
- [3] Ye H, Li Y, Chen J, Sheng J, Fu X-Z, Sun R, Wong C-P (2018) PdCu alloy nanoparticles supported on reduced

- graphene oxide for electrocatalytic oxidation of methanol. *J Mater Sci*. <https://doi.org/10.1007/s10853-018-2759-5>
- [4] Koper MT (2004) Electrocatalysis on bimetallic and alloy surfaces. *Surf Sci*. <https://doi.org/10.1016/j.susc.2003.10.045>
- [5] Ahmed J, Ramanujachary KV, Lofland SE, Furiato A, Gupta G, Shivaprasad SM, Ganguli AK (2008) Bimetallic Cu–Ni nanoparticles of varying composition (CuNi₃, CuNi, Cu₃Ni). *Colloids Surf A*. <https://doi.org/10.1016/j.colsurfa.2008.08.007>
- [6] Huang X, Dai B, Ren Y, Xu J, Zhao C (2015) Controllable synthesis and electromagnetic interference shielding properties of magnetic CoNi alloy nanoparticles coated on bio-carbon nanofibers. *J Mater Sci Mater Electron*. <https://doi.org/10.1007/s10854-015-2727-7>
- [7] You H, Yang S, Ding B, Yang H (2013) Synthesis of colloidal metal and metal alloy nanoparticles for electrochemical energy applications. *Chem Soc Rev*. <https://doi.org/10.1039/C2CS35319A>
- [8] Zhang J, Chaker M, Ma D (2017) Pulsed laser ablation based synthesis of colloidal metal nanoparticles for catalytic applications. *J Colloid Interface Sci*. <https://doi.org/10.1016/j.jcis.2016.07.050>
- [9] Zhang D, Gökce B, Barcikowski S (2017) Laser synthesis and processing of colloids: fundamentals and applications. *Chem Rev*. <https://doi.org/10.1021/acs.chemrev.6b00468>
- [10] Reichenberger S, Marzun G, Muhler M, Barcikowski S (2019) Perspective of surfactant-free colloidal nanoparticles in heterogeneous catalysis. *ChemCatChem*. <https://doi.org/10.1002/cctc.201900666>
- [11] Forsythe RC, Cox CP, Wilsey MK, Müller AM (2021) Pulsed laser in liquids made nanomaterials for catalysis. *Chem Rev*. <https://doi.org/10.1021/acs.chemrev.0c01069>
- [12] Kazakevich PV, Voronov VV, Simakin AV, Shafeev GA (2004) Production of copper and brass nanoparticles upon laser ablation in liquids. *Quantum Electron*. <https://doi.org/10.1070/QE2004v034n10ABEH002756>
- [13] Sukhov IA, Shafeev GA, Voronov VV, Sygletou M, Stratakis E, Fotakis C (2014) Generation of nanoparticles of bronze and brass by laser ablation in liquid. *Appl Surf Sci*. <https://doi.org/10.1016/j.apsusc.2013.12.018>
- [14] Malviya KD, Chattopadhyay K (2014) Synthesis and mechanism of composition and size dependent morphology selection in nanoparticles of Ag–Cu alloys processed by laser ablation under liquid medium. *J Phys Chem C*. <https://doi.org/10.1021/jp502327c>
- [15] Lee I, Han SW, Kim K (2001) Production of Au–Ag alloy nanoparticles by laser ablation of bulk alloys. *Chem Commun (Cambridge, England)*. <https://doi.org/10.1039/B105437F>
- [16] Seto T, Koga K, Akinaga H, Takano F, Orii T, Hirasawa M (2006) Laser ablation synthesis of monodispersed magnetic alloy nanoparticles. *J Nanopart Res*. <https://doi.org/10.1007/s11051-005-9010-4>
- [17] Nadarajah R, Tahir S, Landers J, Koch D, Semisalova AS, Wiemeler J, El-Zoka A, Kim S-H, Utzat D, Möller R, Gault B, Wende H, Farle M, Gökce B (2020) Controlling the oxidation of magnetic and electrically conductive solid-solution iron-rhodium nanoparticles synthesized by laser ablation in liquids. *Nanomaterials (Basel, Switzerland)*. <https://doi.org/10.3390/nano10122362>
- [18] Jakobi J, Menéndez-Manjón A, Chakravadhanula VSK, Kienle L, Wagener P, Barcikowski S (2011) Stoichiometry of alloy nanoparticles from laser ablation of PtIr in acetone and their electrophoretic deposition on PtIr electrodes. *Nanotechnology*. <https://doi.org/10.1088/0957-4484/22/14/145601>
- [19] Mahfouz R, Cadete Santos Aires FJ, Brenier A, Ehret E, Roumié M, Nsouli B, Jacquier B, Bertolini JC (2010) Elaboration and characterization of bimetallic nanoparticles obtained by laser ablation of Ni₇₅Pd₂₅ and Au₇₅Ag₂₅ targets in water. *J Nanopart Res*. <https://doi.org/10.1007/s11051-010-9949-7>
- [20] Censabella M, Torrisi V, Boninelli S, Bongiorno C, Grimaldi MG, Ruffino F (2019) Laser ablation synthesis of mono- and bimetallic Pt and Pd nanoparticles and fabrication of Pt-Pd/Graphene nanocomposites. *Appl Surf Sci*. <https://doi.org/10.1016/j.apsusc.2019.01.029>
- [21] Brandiele R, Amendola V, Guadagnini A, Rizzi GA, Badocco D, Pastore P, Isse AA, Durante C, Gennaro A (2019) Facile synthesis of Pd₃Y alloy nanoparticles for electrocatalysis of the oxygen reduction reaction. *Electrochim Acta*. <https://doi.org/10.1016/j.electacta.2019.134563>
- [22] Löffler T, Waag F, Gökce B, Ludwig A, Barcikowski S, Schuhmann W (2021) Comparing the activity of complex solid solution electrocatalysts using inflection points of voltammetric activity curves as activity descriptors. *ACS Catal*. <https://doi.org/10.1021/acscatal.0c03313>
- [23] Neumeister A, Jakobi J, Rehbock C, Moysig J, Barcikowski S (2014) Monophasic ligand-free alloy nanoparticle synthesis determinants during pulsed laser ablation of bulk alloy and consolidated microparticles in water. *Phys Chem Chem Phys*. <https://doi.org/10.1039/C4CP03316G>
- [24] Okamoto H, Massalski TB (1985) The Au–Pt (Gold–Platinum) system. *Bull Alloy Phase Diagrams*. <https://doi.org/10.1007/BF02871187>
- [25] Zhang J, Oko DN, Garbarino S, Imbeault R, Chaker M, Tavares AC, Guay D, Ma D (2012) Preparation of PtAu alloy colloids by laser ablation in solution and their

- characterization. *J Phys Chem C*. <https://doi.org/10.1021/jp302485g>
- [26] Chen Y-H, Yeh C-S (2001) A new approach for the formation of alloy nanoparticles: laser synthesis of gold–silver alloy from gold–silver colloidal mixtures. *Chem Commun* (Cambridge, England). <https://doi.org/10.1039/B009854J>
- [27] Izgaliev AT, Simakin AV, Shafeev GA, Bozon-Verduraz F (2004) Intermediate phase upon alloying Au–Ag nanoparticles under laser exposure of the mixture of individual colloids. *Chem Phys Lett*. <https://doi.org/10.1016/j.cplett.2004.04.053>
- [28] Compagnini G, Messina E, Puglisi O, Cataliotti RS, Nicolosi V (2008) Spectroscopic evidence of a core–shell structure in the earlier formation stages of Au–Ag nanoparticles by pulsed laser ablation in water. *Chem Phys Lett*. <https://doi.org/10.1016/j.cplett.2008.04.051>
- [29] Besner S, Meunier M (2010) Femtosecond laser synthesis of AuAg nanoalloys: photoinduced oxidation and ions release. *J Phys Chem C*. <https://doi.org/10.1021/jp102461u>
- [30] Amendola V, Scaramuzza S, Carraro F, Cattaruzza E (2017) Formation of alloy nanoparticles by laser ablation of Au/Fe multilayer films in liquid environment. *J Colloid Interface Sci*. <https://doi.org/10.1016/j.jcis.2016.10.023>
- [31] Tymoczko A, Kamp M, Rehbock C, Kienle L, Cattaruzza E, Barcikowski S, Amendola V (2019) One-step synthesis of Fe–Au core–shell magnetic-plasmonic nanoparticles driven by interface energy minimization. *Nanoscale Horiz*. <https://doi.org/10.1039/C9NH00332K>
- [32] Shih C-Y, Chen C, Rehbock C, Tymoczko A, Wiedwald U, Kamp M, Schuermann U, Kienle L, Barcikowski S, Zhigilei LV (2021) Limited elemental mixing in nanoparticles generated by ultrashort pulse laser ablation of AgCu bilayer thin films in a liquid environment: atomistic modeling and experiments. *J Phys Chem C*. <https://doi.org/10.1021/acs.jpcc.0c09970>
- [33] Nishizawa T, Ishida K (1984) The Co–Fe (Cobalt–Iron) system. *Bull Alloy Phase Diagrams*. <https://doi.org/10.1007/BF02868548>
- [34] Goldstein JI, Newbury DE, Michael JR, Ritchie NWM, Scott JHJ, Joy DC (2018). In: Goldstein JI, Newbury DE, Michael JR, Ritchie NW, Scott JHJ, Joy DC (eds) *Scanning electron microscopy and X-ray microanalysis*. Springer New York, New York, pp 39–63
- [35] Waag F, Gökce B, Barcikowski S (2019) Ablation target cooling by maximizing the nanoparticle productivity in laser synthesis of colloids. *Appl Surf Sci*. <https://doi.org/10.1016/j.apsusc.2018.10.030>
- [36] Brorson SD, Kazerooni A, Mooderi JS, Face DW, Cheng TK, Ippen EP, Dresselhaus MS (1990) Femtosecond room-temperature measurement of the electron–phonon coupling constant gamma in metallic superconductors. *Phys Rev Lett*. <https://doi.org/10.1103/PhysRevLett.64.2172>
- [37] Tong Z, Li S, Ruan X, Bao H (2019) Comprehensive first-principles analysis of phonon thermal conductivity and electron–phonon coupling in different metals. *Phys Rev B*. <https://doi.org/10.1103/PhysRevB.100.144306>
- [38] Yao YL, Chen H, Zhang W (2005) Time scale effects in laser material removal: a review. *Int J Adv Manuf Technol*. <https://doi.org/10.1007/s00170-003-2026-y>
- [39] Chichkov BN, Momma C, Nolte S, Alvensleben F, Tünnermann A (1996) Femtosecond, picosecond and nanosecond laser ablation of solids. *Appl Phys A*. <https://doi.org/10.1007/BF01567637>
- [40] Schmitz T, Wiedwald U, Dubs C, Gökce B (2017) Ultra-small yttrium iron garnet nanoparticles with high coercivity at low temperature synthesized by laser ablation and fragmentation of pressed powders. *Chemphyschem A Eur J Chem Phys Phys Chem*. <https://doi.org/10.1002/cphc.201601183>
- [41] Johny J, Li Y, Kamp M, Prymak O, Liang S-X, Krekeler T, Ritter M, Kienle L, Rehbock C, Barcikowski S, Reichenberger S (2021) Laser-generated high entropy metallic glass nanoparticles as bifunctional electrocatalysts. *Nano Res*. <https://doi.org/10.1007/s12274-021-3804-2>
- [42] Amendola V, Riello P, Meneghetti M (2011) Magnetic nanoparticles of iron carbide, iron oxide, iron@iron oxide, and metal iron synthesized by laser ablation in organic solvents. *J Phys Chem C*. <https://doi.org/10.1021/jp109371m>
- [43] Kanitz A, Hoppius JS, Del Mar SM, Maicas M, Ostendorf A, Gurevich EL (2017) Synthesis of magnetic nanoparticles by ultrashort pulsed laser ablation of iron in different liquids. *Chemphyschem A Eur J Chem Phys Phys Chem*. <https://doi.org/10.1002/cphc.201601252>
- [44] Chen GX, Hong MH, Lan B, Wang ZB, Lu YF, Chong TC (2004) A convenient way to prepare magnetic colloids by direct Nd:YAG laser ablation. *Appl Surf Sci*. <https://doi.org/10.1016/j.apsusc.2004.01.007>
- [45] Zhang H, Liang C, Liu J, Tian Z, Shao G (2013) The formation of onion-like carbon-encapsulated cobalt carbide core/shell nanoparticles by the laser ablation of metallic cobalt in acetone. *Carbon*. <https://doi.org/10.1016/j.carbon.2012.12.015>
- [46] Waag F, Li Y, Ziefuß AR, Bertin E, Kamp M, Duppe V, Marzun G, Kienle L, Barcikowski S, Gökce B (2019) Kinetically-controlled laser-synthesis of colloidal high-entropy alloy nanoparticles. *RSC Adv*. <https://doi.org/10.1039/c9ra03254a>
- [47] Burke MS, Kast MG, Trotochaud L, Smith AM, Boettcher SW (2015) Cobalt-iron (oxy)hydroxide oxygen evolution electrocatalysts: the role of structure and composition on

- activity, stability, and mechanism. *J Am Chem Soc.* <https://doi.org/10.1021/jacs.5b00281>
- [48] Smith RDL, Pasquini C, Loos S, Chernev P, Klingan K, Kubella P, Mohammadi MR, Gonzalez-Flores D, Dau H (2017) Spectroscopic identification of active sites for the oxygen evolution reaction on iron–cobalt oxides. *Nat Commun.* <https://doi.org/10.1038/s41467-017-01949-8>
- [49] Stafe M (2012) Theoretical photo-thermo-hydrodynamic approach to the laser ablation of metals. *J Appl Phys.* <https://doi.org/10.1063/1.4771692>

Publisher's Note Springer Nature remains neutral with regard to jurisdictional claims in published maps and institutional affiliations.